

This is the accepted manuscript made available via CHORUS. The article has been published as:

Transport dynamics of superparamagnetic microbeads trapped by mobile magnetic domain walls

E. Rapoport and G. S. D. Beach

Phys. Rev. B **87**, 174426 — Published 24 May 2013

DOI: [10.1103/PhysRevB.87.174426](https://doi.org/10.1103/PhysRevB.87.174426)

Transport Dynamics of Superparamagnetic Microbeads Trapped by Mobile Magnetic Domain Walls

E. Rapoport and G. S. D. Beach*

*Department of Materials Science and Engineering, Massachusetts Institute of Technology,
Cambridge, Massachusetts, 02139*

*E-mail: gbeach@mit.edu

Abstract

The dynamics of fluid-borne superparamagnetic bead transport by field-driven domain walls in submicrometer ferromagnetic tracks is studied experimentally together with numerical and analytical modeling. A combination of micromagnetic modeling and numerical calculation is used to determine the strength of bead-domain wall interaction for a range of track geometries and bead sizes. The maximum domain wall velocity for continuous bead transport is predicted from these results and shown to be supported by experimental measurements. Enhancement of the maximum velocity by appropriate material selection or field application is demonstrated and an analysis of the source of statistical variation is presented. Finally, the dynamics of bead-domain wall interaction and bead transport above the maximum domain wall velocity for continuous domain wall-mediated bead transport is characterized.

1. Introduction

Surface-functionalized superparamagnetic (SPM) microbeads are the biomedical industry workhorse for tagging, manipulating, and detecting chemical and biological species in a fluid environment. Over the past several years, there has been a steady progression in the advancement of magnetic technologies for bead manipulation. In particular, there is great interest in exploiting this functionality in chip-based devices¹⁻³⁰ that reduce the complexity, time, and volume of material required for chemical or biological analysis in, e.g., rapid medical screening applications.

Recent work has shown that, owing to their highly localized stray fields, magnetic domain walls (DWs) are suitable candidates for fast and precise magnetic bead manipulation and detection¹⁹⁻³⁰. Vieira et al.¹⁹ demonstrated that DWs in zig-zag magnetic nanotracks can be used to capture and release SPM microbeads and magnetically tagged entities and shuttle them across the surface of a substrate. Donolato et al.²² extended this work to show that not only could beads follow the travelling DW potential, but that they could precisely track it in a curved structure. In recent results²⁵, we reported on the DW-mediated transport of beads through viscous fluid along curved tracks at speeds approaching 1 mm/s.

On the detection side, it has been shown that DWs can also be used to sense the presence of individual beads^{14,26,28,30}. Llandro et al.¹⁴ demonstrated the detection of individual beads by measuring the effect of their stray field on DW-mediated magnetization switching in pseudo-spin-valves. Vavassori et al.²⁸ exploited the magnetic focusing action of DWs to position a bead near a DW trapped at a nanotrack corner, and then detect the bead's presence based on a small change in the DW depinning field. Both of these mechanisms, though capable of single bead detection, require chemical hybridization between the bead and sensor surface, and are therefore incompatible with simultaneous DW-based bead transport. To address this issue, we recently demonstrated the identification of beads by their magneto-mechanical resonant response^{26,30},

which could in principle be used to identify analyte binding to the bead via changes to hydrodynamic drag, either directly or through secondary bead attachment. Given the range of opportunities for bead manipulation afforded by the bead-DW interaction, a thorough investigation of the system is warranted. This is the aim of the current work.

We first carefully investigate the strength of interaction between a bead and DW. Although several estimates of the binding strength between a wall and trapped bead have been reported^{19,20,23,24,27}, these calculations have generally been limited to model parameters which do not accurately represent the size and magnetic state of the bead-DW system. In this work, we use a combination of micromagnetic modeling and numerical calculation to predict bead-DW interaction forces for experimentally relevant geometries.

From the basis of these force calculations, maximum velocities for DW-mediated SPM microbead transport through a viscous fluid are predicted. Furthermore, the effects of various parameters on such transport are investigated, and experiment is found to agree with prediction. Repeated measurements of maximum velocities are conducted and the distribution of results analyzed. It is found that, given sufficient field, transport is reproducible. Finally, for DWs traveling beyond the maximum velocity, a second “knocking” mode of DW-mediated bead transport is exhibited. The dynamics of this second transport mode is characterized both theoretically and experimentally.

2. Magnetic Bead-DW Interaction

We consider a SPM bead proximate to a submicrometer-wide track of soft magnetic material. Fig. 1(a) shows the geometry of the modeled system. In the soft magnetic track, magnetic domains orient along the length, separated by a DW that generates high-gradient stray magnetic fields, $\mathbf{B}(\mathbf{r})$, due to the strong divergence of the DW magnetization.

Bead capture occurs when the stray field of the DW induces a magnetic moment in the nearby SPM bead, creating a magnetostatic potential well localized at the DW center. The bead-DW interaction force F_{int} , calculated from the energy gradient along the track direction as a function of bead-DW separation, draws the bead toward the DW. Once the bead is trapped in the potential well of the DW, the DW can be used to manipulate individual beads. Indeed, bead transport has been realized by either stepping a bead from one DW trap site to the next^{19,21-24,27} or moving it continuously with a propagating DW^{20,22,25,26}. Continuous transport is limited, however, by the maximum interaction force, or binding force F_{bind} , between the bead and DW, which must overcome the hydrodynamic drag force F_{drag} on the bead as it is pulled through the host fluid²⁰.

In order to investigate the limits of continuous transport, we have calculated the magnetostatic potential energy landscape and binding forces for SPM beads near a DW in a $\text{Ni}_{80}\text{Fe}_{20}$ (Permalloy) nanotrack for a range of bead sizes and track dimensions. The spin configuration of the DW is first computed micromagnetically using the Object-Oriented Micromagnetics Framework (OOMMF) platform³¹. The simulation assumed materials parameters for bulk $\text{Ni}_{80}\text{Fe}_{20}$ (exchange constant $A = 1.3 \times 10^{-11} \text{ J m}^{-1}$, saturation magnetization $M_s = 800 \text{ kA m}^{-1}$, uniaxial anisotropy $K_u = 0$), and used a cell size of $5 \times 5 \times Z \text{ nm}^3$, where $Z = 5$ or 40 nm for 5 or 40 nm thick tracks, respectively. The magnetization profile was used to compute the stray field via the scalar potential. From the stray field, the magnetostatic potential energy of a spherical SPM bead was estimated by integrating the dipolar energy density $-\mathbf{M} \cdot \mathbf{B}$ over the bead volume, assuming a bead magnetization $\mathbf{M} = \chi \mathbf{B} / \mu_0$ with $\chi / \mu_0 = 800 \text{ kA m}^{-1} \text{ T}^{-1}$ ⁵ and a sphere demagnetization factor of $1/3$. Although it is expected that the presence of the bead may cause some distortion of the DW structure, these effects are neglected in the current calculations.

We first considered the effect of DW structure on bead-DW interaction. In thin magnetic tracks, magnetization rotation through the DW is forced in plane, and the DW takes one of two main geometries. In narrower, thinner tracks, transverse walls are favored, whereas in wider, thicker tracks, vortex walls are expected³²⁻³⁴. Figs. 1(b) and 1(c) show the top-down view of the spin configuration in the x-y plane of a head-to-head transverse and vortex DW, respectively, in a 200 nm wide, 5 nm thick Permalloy track. In a track of these dimensions, either a transverse or vortex wall could be observed³³, so a direct comparison of the two DW topologies on bead-DW interaction can be made.

The two wall structures exhibit different stray field profiles, which manifests as a difference in the strength of magnetostatic interaction with a SPM bead. This difference is shown in Figs. 1(f) and 1(g), which show energy surfaces for a 1 μm diameter bead over a transverse and vortex wall, respectively, in a 200 nm wide, 5 nm thick Permalloy track. For the same bead and wire dimensions, the effect of DW topology on the magnetostatic potential energy surface is clearly visible. The potential well is deeper, and thus the binding force is greater, for a bead over a transverse wall than for a bead over a vortex wall. In terms of stray field energy density, the transverse structure is clearly preferred.

In order to increase the strength of interaction, thicker tracks i.e. ones with more magnetic material would be used, but the transverse structure cannot be maintained over a wide range of thicknesses³³. However, as shown in Figs. 1(c) and 1(d), the vortex wall structure is only marginally affected by an increase in track thickness. Moreover, despite having a lower stray field energy density, vortex walls in sufficiently thick tracks exhibit a total stray field energy that is greater than that of a transverse wall in a thinner wire. Fig. 1(h) shows the magnetostatic potential energy surface for a 1 μm diameter bead over a vortex wall in 200 nm wide, 40 nm thick Permalloy track. Compared to that of Fig. 1(g), the well in Fig. 1(h) has approximately the same spatial extent but is more than 20 times deeper. This corresponds to

about a 20-fold increase in binding strength (Fig. 2(a)). This large increase in binding force is a result of the quadratic dependence of bead energy on stray field strength. Both the gradient field and the induced moment of the bead scale with the stray field amplitude, which in turn scale with the wire thickness. Because the stray field scales linearly with the thickness of the wire in this range, in this case, the binding force should increase approximately $8^2 = 64$ times between a 5 and 40 nm thick wire. However, because of saturation effects in the bead, only a 25- to 30-fold increase in binding force is predicted.

Track width and bead diameter also have an effect on the magnetostatic energy well profile. Fig. 1(e) shows a vortex wall in an 800 nm wide, 40 nm thick Permalloy track. The vortex structure is maintained as compared to that of Fig. 1(d), but in agreement with prior work³³ showing DW width proportional to track dimensions, its spatial extent is about 4 times greater. Because the DW in a wider track is larger, for the same size bead, the potential landscape is more sensitive to local DW stray field variation. Fig. 1(j) shows the potential landscape for a 1 μm diameter bead over the DW in Fig. 1(e). Two local minima are now visible, compared to the one in Fig. 1(h). These local minima become even more distinct at smaller bead sizes. In Fig. 1(i), a 350 nm diameter bead probes the DW stray field profile, and in addition to the appearance of fine surface features that reflect the local stray field profile (Fig. 1(i), inset), the reduced overall well depth, compared to that of Fig. 1(j), is also seen. This corresponds to a decrease in magnetic moment due to the decreased bead size. In contrast, for a larger 2.8 μm diameter bead over the same vortex wall of Fig. 1(e), the well is both deeper and more smoothed out (Fig. 1(k)).

Binding strengths between beads and DWs were calculated from these magnetostatic potential energy surfaces. Fig. 2(a) shows binding strength as a function of bead diameter, for beads with diameter D spanning 100 nm to 2 μm , over seven track-DW configurations. F_{bind} , computed as the maximum longitudinal gradient of each potential, increases with D up to $D \sim$

800 nm, then saturates as the stray field falls off with distance from the track. The effect of increasing track thickness on binding force is seen as a greater than order of magnitude increase in F_{bind} for beads over vortex walls in 200 wide tracks, and a less dramatic but still significant variation in F_{bind} with track width is also seen. An optimal track width is observed, which reflects the tradeoff in increased stray field energy due to a larger DW, with the larger spatial extent of the stray field.

Following the model of Bryan *et al.*²⁰, maximum coupled transport speeds, v_{max} , were estimated by equating F_{bind} with viscous drag, assuming Stokes form $F_{drag} = -6\pi\eta\xi rv$ where $r = D/2$, with a viscosity, η , of water (10^{-3} Pa s) and a near surface correction factor $\xi = 2.2$ for a bead dragged parallel to a surface³⁵. As seen in Fig. 2(b), v_{max} increases rapidly with D until F_{bind} plateaus, then falls off as $\sim 1/D$ as viscous drag continues to increase. Over a wide range of D , transport speeds in the mm/s range are predicted.

Higher transport velocities can be achieved by increasing the strength of bead-DW interaction via bead or DW moment enhancement. Due to the primarily out-of-plane stray field from the DW, an additional externally applied out-of-plane field H_z can be used to augment the moment of the bead¹⁹. Magnetostatic potential energy surfaces of a 1 μm diameter bead over the DW of Fig. 1(d) were calculated as a function of H_z and the longitudinal cross sections of these surfaces are shown in Fig. 3(a). As expected, the increased moment of the bead leads to a stronger bead-DW interaction in the form of a deepening well. Conversely, an applied field of reverse polarity can be used to decrease the strength of bead-DW interaction. A plot of the binding force from these surfaces (Fig. 3(b)) shows a linear relationship between F_{bind} and out-of-plane field in a range in which the effect of field on the domain wall structure can be neglected. Furthermore, a higher saturation magnetization track material, such as CoFe, would enhance the moment of the DW and thus increase bead-DW magnetostatic interaction and

binding forces. Thus, application of an out-of-plane field or use of a higher M_s material can be used to increase maximum transport speeds.

3. Maximum velocity measurement

To verify predicted transport velocities for DW-mediated bead transport through a viscous medium, maximum velocities were measured experimentally. In order to have fine control over the DW velocity, a circular geometry was chosen for the magnetic tracks. In such structures, the DW velocity can be precisely clocked with a rotating field. Arrays of $\text{Ni}_{80}\text{Fe}_{20}$ (40 nm)/ Pt (2 nm) and Cu (2.5 nm)/ $\text{Co}_{50}\text{Fe}_{50}$ (40 nm)/ Pt (2 nm) circular tracks on a Si(100) wafer were prepared by electron beam lithography, dc sputtering, and liftoff. The Cu underlayer of the CoFe tracks was used to reduce the coercivity in the CoFe layer³⁶. Each track was 800 nm wide and 20 μm in diameter. After patterning, the wafers were coated with a 70 nm thick rf-sputtered protective SiO_2 overlayer. Experiments were performed using commercial Dynabeads M270 Carboxylic Acid SPM beads from Dynal Biotech, with mean diameter 2.8 μm . Beads were suspended in water at a concentration of 10^5 beads/mL.

Prior to experiments, a large in-plane magnetic field was applied to coerce the tracks into an “onion” domain configuration, with two circumferential magnetic domains separated by DWs lying along the field axis^{34,37-40}. A dilute suspension of SPM beads was then placed in a polydimethylsiloxane (PDMS) well on the wafer surface and sealed with a microscope cover slip. Bead capture by DW fringing fields was monitored via a CCD camera fitted to a custom microscope apparatus. Beads far from the tracks executed a Brownian random walk across the wafer surface, but those wandering to within ~ 10 μm of a track were abruptly drawn towards and trapped by the nearest DW. A significant number of capture events typically occurred across the array within a few minutes of bead introduction.

Magnetic fields were applied using a custom-built compact projection electromagnet capable of producing vector in-plane fields of up to 500 Oe with a bandwidth > 1 kHz. The

dynamic response of individual trapped beads was tracked using a CCD camera fitted to an imaging microscope (Mitutoyo 10x M Plan APO) integrated with a custom LabVIEW imaging program. In previous work²⁵, we investigated the motion of individual 1 μm diameter trapped beads by monitoring the reflected light intensity from a focused laser spot as the bead passed underneath the beam. Here, we interface to the CCD camera with a LabVIEW program that allows for region of interest (ROI) definition. The ROI replaces the laser of previous work, and ROI pixel information substitutes reflected laser light intensity.

The image in Fig. 4(a) shows a single 2.8 μm diameter bead trapped by a DW in a circular Permalloy ring. An in-plane rotating field was used to drive the bead-DW pair around the ring, and the pair followed the field axis with a direction consistent with the sense of field rotation. With an ROI (typically $\sim 5 \times 5 \mu\text{m}^2$) positioned on the track perimeter, and the CCD frame rate set at 70 frames per second (fps), pixel intensity in the ROI was monitored in time. Bead traversal through the ROI was accompanied by a dip in pixel intensity. Real time single-shot measurement of dip frequency, corresponding to bead frequency f_{bead} around the ring, was taken as the drive field rotation frequency f_{drive} was slowly ramped up to ~ 30 Hz. Taking the linear bead and DW velocity as $v_{\text{bead}} = 2\pi R f_{\text{bead}}$ and $v_{\text{DW}} = 2\pi R f_{\text{drive}}$, respectively, bead velocity versus DW velocity (VV) curves were plotted. With this technique, a maximum observable bead velocity of $\frac{2\pi R}{1/(\text{frame rate})} \sim 4400 \mu\text{m/s}$ could be measured. The results of velocity measurements taken under different conditions are shown in Figs. 4(b)-(d).

Fig. 4(b) investigates the effect of bead size and compares a VV curve for a 2.8 μm diameter bead to that of a 1 μm diameter Dynabeads MyOne Carboxylic Acid SPM bead²⁵. Both beads exhibit two clear regimes in their VV curves. At low DW velocities, there is a linear relationship between bead and DW velocity, corresponding to continuous DW-mediated bead transport by a single DW. This regime functions at DW velocities below v_{max} . Above v_{max} ,

bead velocity falls off precipitously with DW velocity. This second regime will be the discussion of the next section.

The difference in the two curves is due to the difference in bead size. From the calculations of binding force as a function of bead diameter (Fig. 2(a)), it is expected that these beads should have similar binding forces with the DW, and that their v_{max} should be approximately inversely proportional to their radii. Indeed this is observed, with the large and small beads reaching v_{max} of 290 and 925 $\mu\text{m/s}$, respectively, and provides a means to distinguish beads based on their size.

Next, out-of-plane fields were applied to increase the moment and thus the maximum velocities of beads, as per the discussion in Section 2. The VV curve of the same 2.8 μm diameter bead in zero and non-zero ($H_z = 250$ Oe) out-of-plane field (Fig. 4(c)) shows a 2-fold enhancement of v_{max} . We can compare these results to those of Fig. 3(b), which show an approximately 3-fold increase in F_{bind} for a 1 μm diameter bead over a vortex wall in a 200 nm wide, 40 nm thick Permalloy track in a 250 Oe field. Since for a given size bead F_{drag} does not change with H_z , v_{max} should scale directly with F_{bind} . Fig. 3(b) thus predicts a 3-fold increase in v_{max} at this H_z , which is somewhat larger than the 2-fold increase observed experimentally. Since the slope of binding force vs. H_z is proportional to the susceptibility, the quantitative discrepancy can likely be attributed to a difference in the susceptibility of this bead compared to the value used in simulations. Despite quantitative differences, the experimental results are in good qualitative agreement with calculation, and show a clear maximum velocity enhancement by application of an out-of-plane field.

Finally, the effect of track material was investigated. As mentioned in the previous section, an increase in saturation magnetization of the track should result in a larger binding force. Fig. 4(d) plots the VV curves of two 2.8 μm diameter beads driven around CoFe

($M_s=1910 \text{ kA m}^{-1}$)⁴¹ and NiFe ($M_s=800 \text{ kA m}^{-1}$)²⁰ rings of the same dimensions. The bead on the CoFe ring exhibits a v_{max} (785 $\mu\text{m/s}$) higher than that of the bead on the NiFe ring, proportional to the ratio of M_s between the two materials.

VV curves for 28 beads on CoFe and 30 on NiFe rings were measured and the maximum velocity distributions for these two populations can be seen in Fig. 5(a). The data show a narrow distribution for the beads on NiFe rings, centered on a mean at 273 $\mu\text{m/s}$ with a standard deviation of 6 $\mu\text{m/s}$. For beads on CoFe rings, however, the average velocity is 539 $\mu\text{m/s}$ with standard deviation 24 $\mu\text{m/s}$. The average upward shift in v_{max} is consistent with the data shown in Fig. 4(c), but the significantly larger standard deviation in v_{max} for these beads compared to that of beads over NiFe is unexpected given that the beads and surfaces used for both these measurements were nominally the same.

The difference in standard deviation is understood through an analysis of maximum velocity versus drive field amplitude. This relationship reflects the influence of pinning on domain wall propagation around the rings. Hysteresis loops measured on continuous films exhibit coercivities of $\sim 1 \text{ Oe}$ for Permalloy and $\sim 10 \text{ Oe}$ for Cu/CoFe. Domain wall pinning due to lithographic defects in the patterned rings is likewise expected to be larger in the CoFe rings than in the Permalloy rings. As DWs are driven around the tracks, they encounter lithographically induced defects. The magnetostatic stray fields in the vicinity of such defects create local potentials that act as pinning sites for DWs⁴². Given that the stray field strength scales with the track material M_s , for the same landscape, a DW should experience stronger pinning in a higher M_s material track. It follows that a DW will encounter stronger pinning sites as it is driven around a CoFe track than around a NiFe one, such that larger drive field amplitudes will be necessary to move DWs smoothly through the former than the latter. Below the threshold field for smooth DW motion, DWs exhibit jagged motion. The DW is repeatedly pinned by defects and subsequently depinned by the increasing tangential component of field as

the lag between the field axis and DW position increases. During depinning, as the DW accelerates to overcome the lag between the DW and field axis, the instantaneous linear velocity of the DW is greater than that of the field axis. For sufficiently large lags, the instantaneous DW velocity exceeds the maximum bead transport velocity, despite the average DW velocity being lower than v_{max} . Negoita *et al.*⁴² studied the motion of DWs in lithographically patterned NiFe rings of similar dimensions and found that the field-DW lag increases with both decreasing field amplitude and increasing field frequency. Thus, one should observe a decrease in maximum bead velocity with decreasing drive field amplitude below threshold.

The maximum velocity versus field curves for two 2.8 μm diameter beads over NiFe tracks (Fig. 5(b)) are consistent with this analysis, showing a constant v_{max} above⁴³ and a decreasing v_{max} below threshold. Curves taken for two beads over CoFe tracks exhibit the same trend below threshold. Due to limitations of the electromagnet used in experiment, however, only field amplitudes below threshold for CoFe rings could be generated. As a result, while the 295 Oe field used to measure v_{max} for beads over both NiFe and CoFe rings is above threshold for NiFe, it is below for CoFe, such that the measured velocities were subject to the local pinning profiles of each circular track used. Thus, the insufficient field amplitude used to measure beads on CoFe rings is likely the cause of the wide distribution in v_{max} (Fig. 5(a)).

4. Beyond the maximum velocity limit

Recalling Fig. 4(b) (reproduced here in Fig. 6(a)) we observe a decreased but finite average bead velocity for DWs traveling above the critical velocity for continuous transport, v_{max} . To explain this observation, we proposed the following model of bead-DW interaction in the high- v_{DW} regime (Fig. 6(b)). As a DW approaches the bead, it pulls the bead abruptly back, resulting in a short negative bead displacement. After its initial backward motion into the potential well, the trapped bead travels with the propagating DW until it is eventually ripped out of the well by viscous drag that exceeds the bead-DW binding force. This longer forward travel results in

overall forward displacement of the bead due to its interaction with the passing DW. A rapid train of DWs could thus propel a bead along a track even if their speed exceeds v_{max} .

We analytically model this response of a bead to a passing DW in a circular track of radius R . The analysis is limited to the x-axis i.e. the axis of motion, because no forces act on the bead in the transverse (y) or, in our simplified model, in the z direction. The DW magnetostatic potential energy surface is approximated as a truncated parabolic well with half width Δ , and $x_{DW}(t)$ and $x_{bead}(t)$ are defined as the position of the well and bead as a function of time, respectively (Fig. 6(c)).

When the DW approaches the bead, it interacts with the bead via the restoring interaction force,

$$F_{int} = k(x_{DW}(t) - x_{bead}(t)), \quad (1)$$

with restoring force constant k . As the bead is forced through the liquid by the DW, it also experiences a strong counteracting damping force from the hydrodynamic drag, which can be written as

$$F_{drag} = -b \frac{dx_{bead}(t)}{dt}, \quad (2)$$

where $b = 6\pi\eta\xi r$ is the composite drag coefficient. Letting time $t = 0$ be when the well first begins interacting with the bead (placed at the origin) such that $x_{bead}(0) = 0$ and $x_{DW}(0) = -\Delta$, and taking an equilibrium approximation of the bead and approaching DW, we can describe the interaction with the following force balance equation:

$$0 = k(v_{DW}t - \Delta - x_{bead}(t)) - b \frac{dx_{bead}(t)}{dt}, \quad (3)$$

where v_{DW} is the DW velocity. This expression can then be solved for $x_{bead}(t)$ to get the following:

$$x_{bead}(t) = v_{DW}t - \Delta - \frac{bv_{DW}}{k} + \frac{k\Delta + bv_{DW}}{k} e^{\frac{-kt}{b}}. \quad (4)$$

Eq. 4 gives the position of a bead interacting with an approaching DW as a function of time. Thus, bead displacement δ due to a passing DW can be expressed as $\delta = x_{bead}(\tau_{int})$, where the interaction time, τ_{int} can be written as

$$\tau_{int} = \frac{2\Delta + \delta}{v_{DW}}. \quad (5)$$

Recognizing that the bead is traveling at its maximum velocity $v_{max} = \frac{k\Delta}{b}$ just before it comes out of the well, we can solve for δ :

$$\delta = -\Delta \left(2 + \frac{v_{DW}}{v_{max}} \ln \left(\frac{v_{DW} - v_{max}}{v_{DW} + v_{max}} \right) \right). \quad (6)$$

To express the bead transport velocity in terms of the DW velocity, we recognize that

$$\delta = \frac{v_{bead}}{\left(\frac{v_{DW}}{\pi R} \right)}, \quad (7)$$

such that the average bead velocity in the high- v_{DW} regime is given as:

$$v_{bead} = -\frac{v_{DW}\Delta}{\pi R} \left(2 + \frac{v_{DW}}{v_{max}} \ln \left(\frac{v_{DW} - v_{max}}{v_{DW} + v_{max}} \right) \right). \quad (8)$$

In agreement with observation (Fig. 6(a)), the model predicts finite bead velocities even when $v_{DW} > v_{max}$. Furthermore, using Eq. 4, we can plot the expected trajectory for a bead interacting with a DW in the high- v_{DW} regime. Fig. 7(a) shows several simulated trajectories of a 2.8 μm diameter bead driven by a vortex DW in a 800 nm wide, 40 nm thick track at various f_{drive} corresponding to velocities above v_{max} . The k and Δ values used were obtained from the simulated potential energy well for this system (Fig. 1(k)). Each trajectory is characterized by a step-like behavior corresponding to the periodic displacement of a bead by passing DWs, as described in Fig. 6(b). A closer look at one of the steps (Fig. 7(a), inset) shows the short backward displacement of a bead as it falls into the well of an approaching DW, followed by a

longer forward travel before detachment from the traveling DW potential. Both the average step size per DW and bead velocity decrease with increasing DW frequency, as per Eq. 7 and Eq. 8, respectively.

These dynamics of bead motion due to passing DWs traveling faster than v_{max} were experimentally confirmed using the optical setup described in Section 3. Videos of bead motion at 60 fps taken at various f_{drive} were analyzed using a custom LabVIEW program that detected the particle and tracked its position over time. To ensure that only absolute bead motion was tracked, wafer vibration was removed by subtracting the position of a stationary reference point from that of the bead for each frame.

Fig. 7(b) shows the experimental trajectories of a 2.8 μm diameter bead driven by a DW in a 800 nm wide, 40 nm thick track at six different drive field frequencies spanning both the low and high DW velocity regimes. In the low DW velocity regime (below the maximum frequency for continuous bead transport $f_{max} = \frac{v_{max}}{2\pi R} \sim 4.5$ Hz), bead position around the ring changes linearly in time. An increase in drive field frequency also results in a corresponding increase in slope i.e. overall bead velocity v_{bead} . Above f_{max} , however, slope decreases with increasing f_{drive} , and periodic stepwise motion develops. That the step period is twice that of f_{drive} , commensurate with the circulation of the two DWs, and the features and trends of the trajectories closely match those of the simulated results, are evidence corroborating the model above.

A significant difference between the simulated and experimental trajectories is observed, however, in the time between DW passings. The simulated results exhibit plateaus between steps, suggesting that the bead sits stationary for some period of time between dislodgement from one DW and capture by the next. The experimental trajectories reveal a lack of such plateau behavior. This, along with observations of bead capture by DWs up to $\sim 10 \mu\text{m}$ away (Section 3), suggests that the tail of bead-DW interaction beyond the truncated well half-width is not

insignificant.

The significance of the bead-DW interaction tail is also evidenced in the fit to the high- v_{DW} points of the VV curve of Fig. 6(a). The solid black line represents the fit, with fitting parameters $\Delta = 49 \mu\text{m}$ and $v_{max} = 227 \mu\text{m/s}$. v_{max} is in relatively good agreement with the data and the fit curve qualitatively reproduces the experimental results. If compared to the potential well of Fig. 1(k), Δ , however, is much larger than expected. This large Δ is attributed to simplification of the well shape to that of a truncated parabolic well. Under this approximation, the tail of bead-DW interaction beyond the Δ distance is ignored. Thus, in fitting experimental results, unrealistically large Δ values are more appropriate to account for the effect from the bead-DW interaction tail.

Finally, we investigated the bead displacement per DW as a function of drive field amplitude. As seen in Fig. 8, for a given field amplitude, bead displacement decreases with increasing v_{DW} or f_{drive} , due to the decreasing interaction time of the bead with the wall (Eq. 6). For a given f_{drive} , as the drive field amplitude is lowered, displacement per DW remains approximately constant till around the threshold field amplitude, below which it falls off. At the limit of very low drive field amplitude, displacement per DW appears to plateau on a constant value. This trend is consistent with the data of Fig. 5(b), in which maximum velocity falls off below threshold due to increased DW pinning.

In this work, the transport dynamics of bead motion along circular tracks has been investigated. In earlier work^{25,26}, we demonstrated that this curved geometry can be extended into a curvilinear backbone to design long-distance linear transport conduits driven by a rotating magnetic field. The knocking transport mode, however, also has implications for moving beads along simpler geometries such as straightaways, where DWs travel much faster than v_{max} . Here, one could imagine a scheme whereby a train of high speed DWs periodically injected into a straight wire at high frequency results in the net displacement of a bead. This, in addition to the

added ability to tailor bead step size per passing DW by application of the appropriate field, is promising for fine bead positioning along tracks of arbitrary geometry.

5. Conclusion

A thorough picture of the interaction between magnetic DWs and SPM microbeads has been presented. Calculation and experiment show a strong magnetostatic binding between bead and DW which is a function of track and bead size, and that can be used to transport beads at very high velocities. Ranges of maximum velocity for a particular bead-DW pair can be tailored by appropriate selection of track material and application of out-of-plane fields, which could be useful in navigating bead populations in real devices. Moreover, there is very little variation in behavior among a population of nominally identical bead-DW pairs under the same conditions. Beyond the maximum velocity for continuous bead transport, there is a knocking mode in which a train of continuously passing DWs can be used to translate a bead by incremental steps whose size is dependent on the drive field amplitude.

This ability to affect maximum transport velocities experimentally and achieve different transport modes in circular and potentially straight geometries demonstrates the inherent richness and flexibility of the bead-DW interaction. In conjunction with the capability for resonant detection of individual beads^{26,30}, the bead-DW system has exciting and promising application in future lab-on-a-chip technologies.

Acknowledgements

This work was supported by the Massachusetts Institute of Technology (MIT) Center for Materials Science and Engineering and Deshpande Center for Technological Innovation. Device fabrication was carried out at MIT's NanoStructures Laboratory. The authors gratefully acknowledge David Bono and Mike Tarkanian for technical assistance.

References

- ¹ Q.A. Pankhurst, J. Connolly, S.K. Jones, and J. Dobson, *J. Phys. D: Appl. Phys.* **36**, R167 (2003).
- ² M.A.M. Gijs, F. Lacharme, and U. Lehmann, *Chem. Rev.* **110**, 1518 (2010).
- ³ T. Deng, M. Prentiss, and G.M. Whitesides, *Appl. Phys. Lett.* **80**, 461 (2002).
- ⁴ N. Pamme and C. Wilhelm, *Lab Chip* **6**, 974 (2006).
- ⁵ R.J.S. Derks, A. Dietzel, R. Wimberger-Friedl, and M.W.J. Prins, *Microfluid. Nanofluid.* **3**, 141 (2007).
- ⁶ B.B. Yellen, R.M. Erb, H.S. Son, R. Hewlin Jr, H. Shang, and G.U. Lee, *Lab Chip* **7**, 1681 (2007).
- ⁷ J.D. Adams, U. Kim, and H.T. Soh, *Proc. Natl. Acad. Sci. USA* **105**, 18165 (2008).
- ⁸ C. Liu, T. Stakenborg, S. Peeters, and L. Lagae, *J. Appl. Phys.* **105**, 102014 (2009).
- ⁹ L. Johansson, K. Gunnarsson, S. Bijelovic, K. Eriksson, A. Surpi, E. Göthelid, P. Svedlindh, and S. Oscarsson, *Lab Chip* **10**, 654 (2010).
- ¹⁰ D. Issadore, H. Shao, J. Chung, A. Newton, M. Pittet, R. Weissleder, and H. Lee, *Lab Chip* **11**, 147 (2011).
- ¹¹ D. Kirby, J. Siegrist, G. Kijanka, L. Zavattoni, O. Sheils, J. O’Leary, R. Burger, and J. Duce, *Microfluid. Nanofluid.* **13**, 899 (2012).
- ¹² D.R. Baselt, G.U. Lee, M. Natesan, S.W. Metzger, P.E. Sheehan, and R.J. Colton, *Biosens. Bioelectron.* **13**, 731 (1998).
- ¹³ H.A. Ferreira, F.A. Cardoso, R. Ferreira, S. Cardoso, and P.P. Freitas, *J. Appl. Phys.* **99**, 1 (2006).
- ¹⁴ J. Llandro, T.J. Hayward, D. Morecroft, J.A.C. Bland, F.J. Castaño, I.A. Colin, and C.A. Ross, *Appl. Phys. Lett.* **91**, 203904 (2007).
- ¹⁵ S.J. Osterfeld, H. Yu, R.S. Gaster, S. Caramuta, L. Xu, S.-J. Han, D.A. Hall, R.J. Wilson, S. Sun, R.L. White, R.W. Davis, N. Pourmand, and S.X. Wang, *Proc. Natl. Acad. Sci. USA* **105**, 20637 (2008).

- ¹⁶ B.T. Dalslet, C.D. Damsgaard, M. Donolato, M. Strømme, M. Strömberg, P. Svedlindh, and M.F. Hansen, *Lab Chip* **11**, 296 (2011).
- ¹⁷ M. Donolato, E. Sogne, B.T. Dalslet, M. Cantoni, D. Petti, J. Cao, F.A. Cardoso, S. Cardoso, P.P. Freitas, M.F. Hansen, and R. Bertacco, *Appl. Phys. Lett.* **98**, 073702 (2011).
- ¹⁸ R.S. Gaster, D.A. Hall, and S.X. Wang, *Lab Chip* **11**, 950 (2011).
- ¹⁹ G. Vieira, T. Henighan, A. Chen, A.J. Hauser, F.Y. Yang, J.J. Chalmers, and R. Sooryakumar, *Phys. Rev. Lett.* **103**, 128101 (2009).
- ²⁰ M.T. Bryan, J. Dean, T. Schrefl, F.E. Thompson, J.W. Haycock, and D.A. Allwood, *Appl. Phys. Lett.* **96**, 192503 (2010).
- ²¹ G. Ruan, G. Vieira, T. Henighan, A. Chen, D. Thakur, R. Sooryakumar, and J.O. Winter, *Nano Lett.* **10**, 2220 (2010).
- ²² M. Donolato, A. Torti, N. Kostasheva, M. Deryabina, E. Sogne, P. Vavassori, M.F. Hansen, and R. Bertacco, *Lab Chip* **11**, 2976 (2011).
- ²³ A. Chen, G. Vieira, T. Henighan, M. Howdyshell, J. North, A.J. Hauser, F.Y. Yang, M. Poirier, C. Jayaprakash, and R. Sooryakumar, *Phys. Rev. Lett.* **107**, 087206 (2011).
- ²⁴ M. Donolato, F. Lofink, S. Hankemeier, J.M. Porro, H.P. Oepen, and P. Vavassori, *J. Appl. Phys.* **111**, 07B336 (2012).
- ²⁵ E. Rapoport and G.S.D. Beach, *Appl. Phys. Lett.* **100**, 082401 (2012).
- ²⁶ E. Rapoport, D. Montana, and G.S.D. Beach, *Lab Chip* **12**, 4433 (2012).
- ²⁷ A. Torti, V. Mondiali, A. Cattoni, M. Donolato, E. Albisetti, A.M. Haghiri-Gosnet, P. Vavassori, and R. Bertacco, *Appl. Phys. Lett.* **101**, 142405 (2012).
- ²⁸ P. Vavassori, V. Metlushko, B. Ilic, M. Gobbi, M. Donolato, M. Cantoni, and R. Bertacco, *Appl. Phys. Lett.* **93**, 203502 (2008).
- ²⁹ M. Donolato, M. Gobbi, P. Vavassori, M. Leone, M. Cantoni, V. Metlushko, B. Ilic, M. Zhang, S.X. Wang, and R. Bertacco, *Nanotechnology* **20**, 385501 (2009).
- ³⁰ E. Rapoport and G.S.D. Beach, *J. Appl. Phys.* **111**, 07B310 (2012).

- ³¹ M.J. Donahue and D.G. Porter, (1999).
- ³² R.D. McMichael and M.J. Donahue, IEEE Trans. Magn. **33**, 4167 (1997).
- ³³ Y. Nakatani, A. Thiaville, and J. Miltat, J. Magn. Magn. Mater. **290-291**, 750 (2005).
- ³⁴ M. Laufenberg, M. Kläui, D. Backes, W. Buhrer, H. Ehrke, D. Bedau, U. Rüdiger, F. Nolting, L.J. Heyderman, S. Cherifi, A. Locatelli, R. Belkhou, S. Heun, C.A.F. Vaz, J.A.C. Bland, T. Kasama, R.E. Dunin-Borkowski, A. Pavlovskaya, and E. Bauer, Adv. in Solid State Phys. **46**, 281 (2008).
- ³⁵ J. Happel and H. Brenner, *Low Reynolds Number Hydrodynamics: with Special Applications to Particulate Media* (Martinus Nijhoff Publishers, 1983).
- ³⁶ H.S. Jung, W.D. Doyle, and S. Matsunuma, J. Appl. Phys. **93**, 6462 (2003).
- ³⁷ J. Rothman, M. Kläui, L. Lopez-Diaz, C.A.F. Vaz, A. Bleloch, J.A.C. Bland, Z. Cui, and R. Speaks, Phys. Rev. Lett. **86**, 1098 (2001).
- ³⁸ F.J. Castaño, C.A. Ross, C. Frandsen, A. Eilez, D. Gil, H.I. Smith, M. Redjda, and F.B. Humphrey, Phys. Rev. B **67**, 184425 (2003).
- ³⁹ M.H. Park, Y. Hong, B.C. Choi, M.J. Donahue, H. Han, and S.H. Gee, Phys. Rev. B **73**, 094424 (2006).
- ⁴⁰ C.A. Ross, F.J. Castaño, W. Jung, B.G. Ng, I.A. Colin, and D. Morecroft, J. Phys. D: Appl. Phys. **41**, 113002 (2008).
- ⁴¹ V.S.N. Murthy, C. Krishnamoorthi, R. Mahendiran, and A.O. Adeyeye, J. Appl. Phys. **105**, 023916 (2009).
- ⁴² M. Negoita, T.J. Hayward, and D.A. Allwood, Appl. Phys. Lett. **100**, 072405 (2012).
- ⁴³ We have calculated the binding energy under application of an in-plane magnetic field transverse to the track and find no significant change, due to the predominantly out-of-plane gradient of the DW stray field.

Figures

Figure 1. (Color online) (a) Schematic of bead-DW interaction showing magnetostatic potential well and relevant forces during DW-mediated transport. (b-e) Micromagnetically calculated DW topology as a function of width and thickness in a Permalloy track, with (b) transverse wall in 200 nm wide, 5 nm thick track; (c) vortex wall in 200 nm wide, 5 nm thick track; (d) vortex wall in 200 nm wide, 40 nm thick track; and (e) vortex wall in 800 nm wide, 40 nm thick track. (f-k) Magnetostatic potential energy surfaces for (f) 1 μm diameter bead over track (b); (g) 1 μm diameter bead over track (c); (h) 1 μm diameter bead over track (d); (i) 350 nm diameter bead over track (e); (j) 1 μm diameter bead over track (e); (k) 2.8 μm diameter bead over track (e).

Figure 2. (a) Calculated longitudinal magnetostatic binding force and (b) maximum coupled transport velocity versus bead diameter for several track dimensions and wall topologies.

Figure 3. (a) Calculated cross sectional profiles of magnetostatic potential energy wells and (b) longitudinal binding forces for a 1 μm diameter bead over a vortex wall in a 200 nm wide, 40 nm thick Permalloy track as a function of out-of-plane applied field.

Figure 4. (Color online) (a) 2.8 μm diameter bead trapped by a DW in a circular 20 μm outer diameter, 800 nm wide, 40 nm thick Permalloy track. Bead versus DW velocity curves as a function of (b) bead diameter, (c) out-of-plane applied field, and (d) track material.

Figure 5. (Color online) (a) Distribution of maximum transport velocities measured for 2.8 μm diameter beads over NiFe and CoFe tracks. (b) Maximum velocities for two beads over each of NiFe and CoFe tracks as a function of applied field amplitude. Lines are meant as guides to the eye.

Figure 6. (Color online) (a) Bead velocity versus DW velocity for a 2.8 μm diameter bead over a 20 μm outer diameter, 800 nm wide, 40 nm thick Permalloy track (reproduced from Fig. 4). (b) Schematic of bead-DW interaction in the high DW velocity regime. (c) Schematic of model bead-DW system, with truncated potential well of half width Δ .

Figure 7. (a) Simulated and (b) experimental trajectories of bead motion due to DW-mediated transport as a function of drive field frequency. Simulation parameters correspond to those calculated for the experimental system. Experimental data shows trajectories at DW frequencies spanning the low and high DW velocity regimes.

Figure 8. Displacement of a $2.8\text{ }\mu\text{m}$ diameter bead by a vortex wall traveling faster than the maximum velocity for continuous transport as a function of drive field amplitude, for several drive field frequencies. Wall in a $20\text{ }\mu\text{m}$ outer diameter, 800 nm wide, 40 nm thick Permalloy track

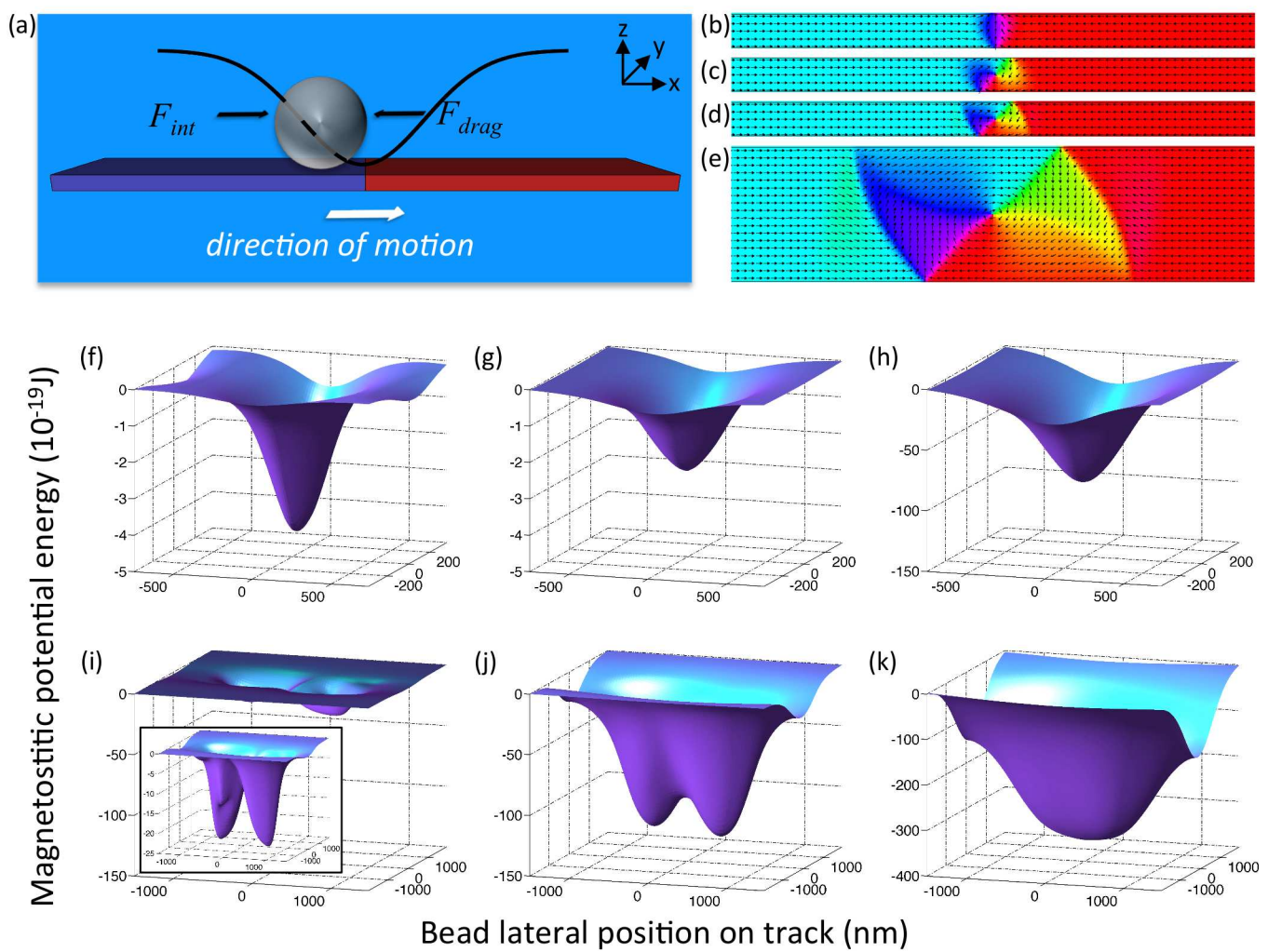


Figure 1

BB11981

30APR2013

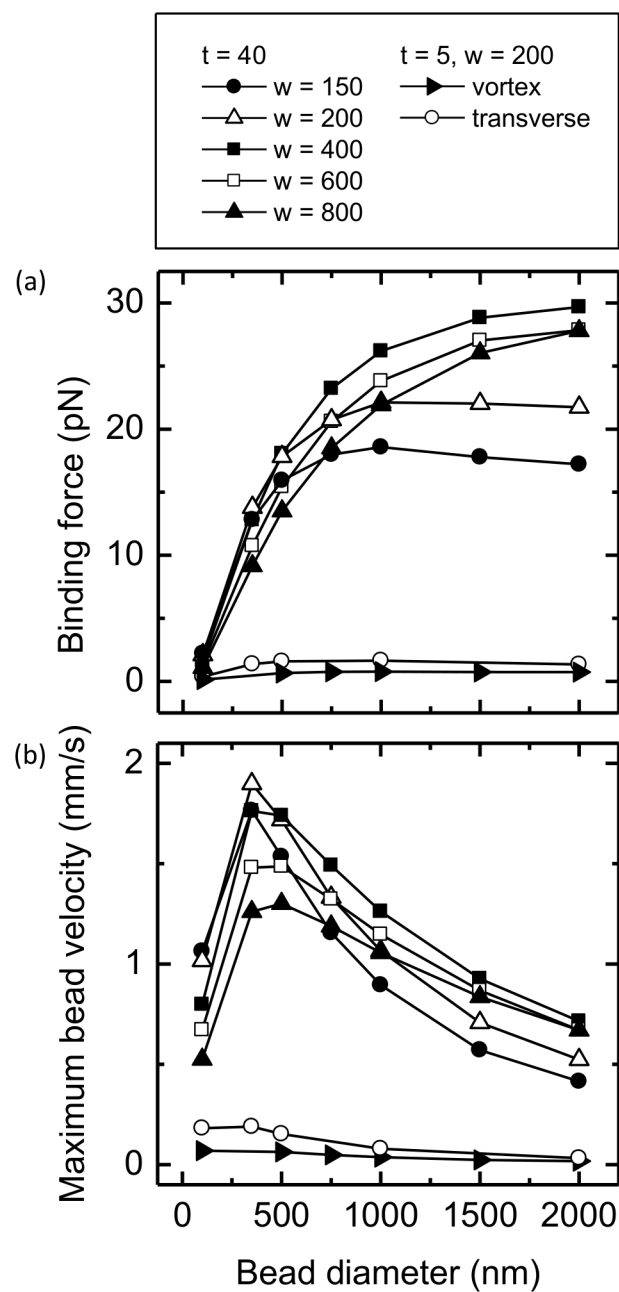


Figure 2

BB11981

30APR2013

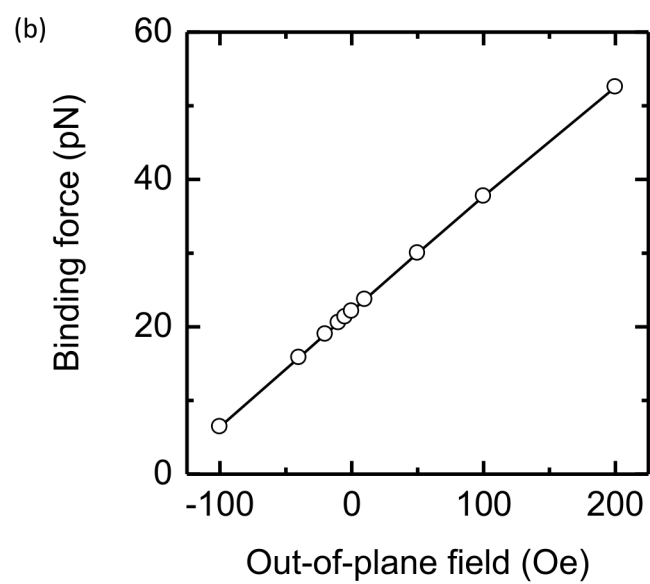
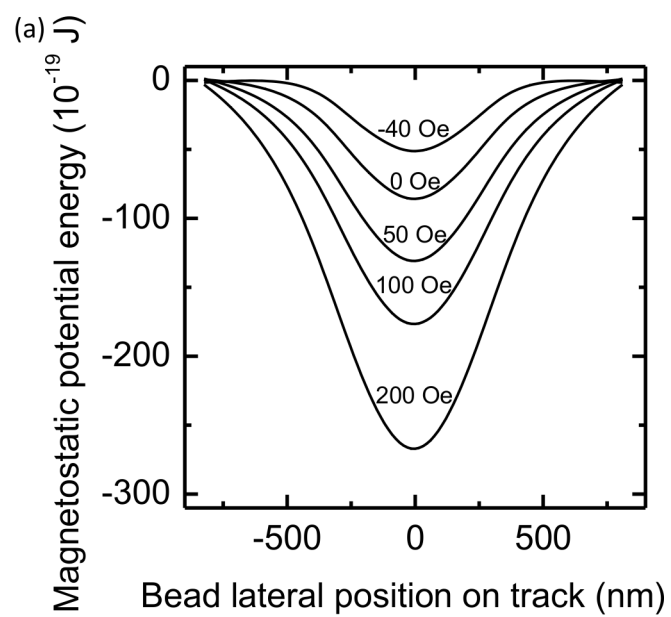
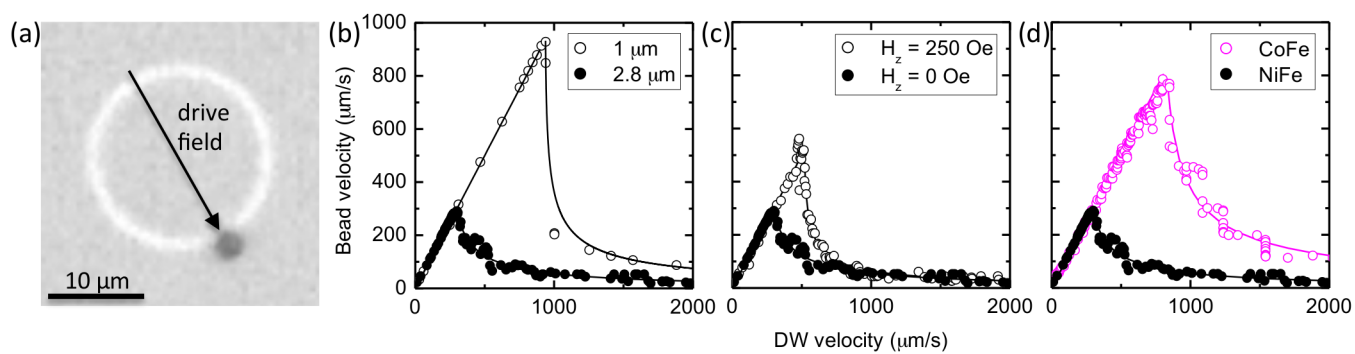


Figure 3

BB11981

30APR2013



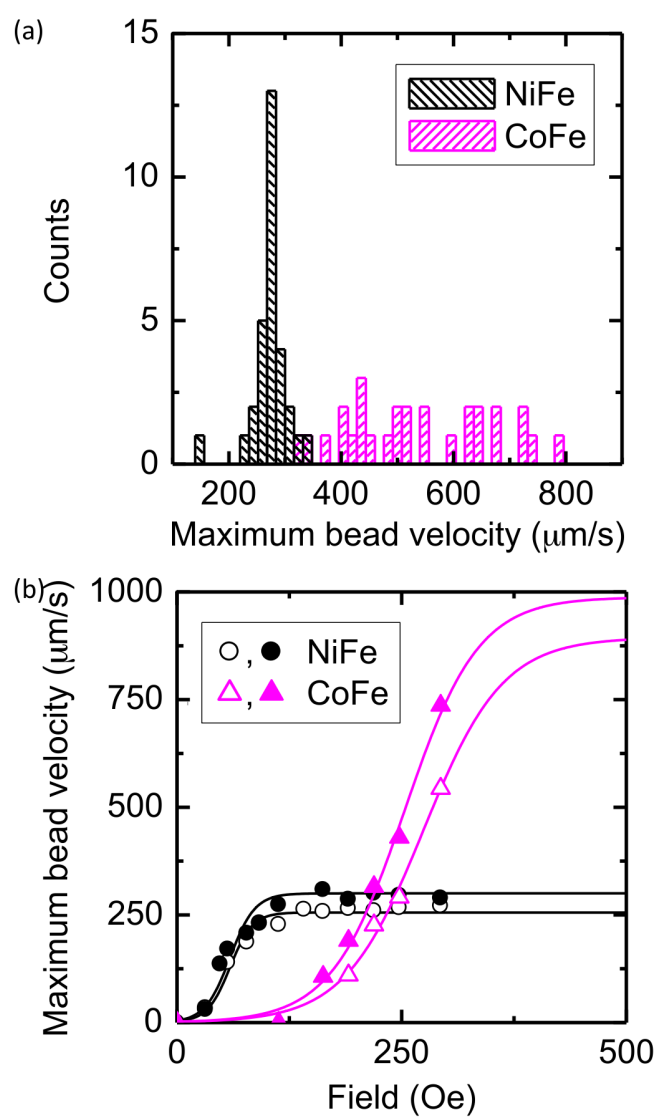


Figure 5

BB11981 30APR2013

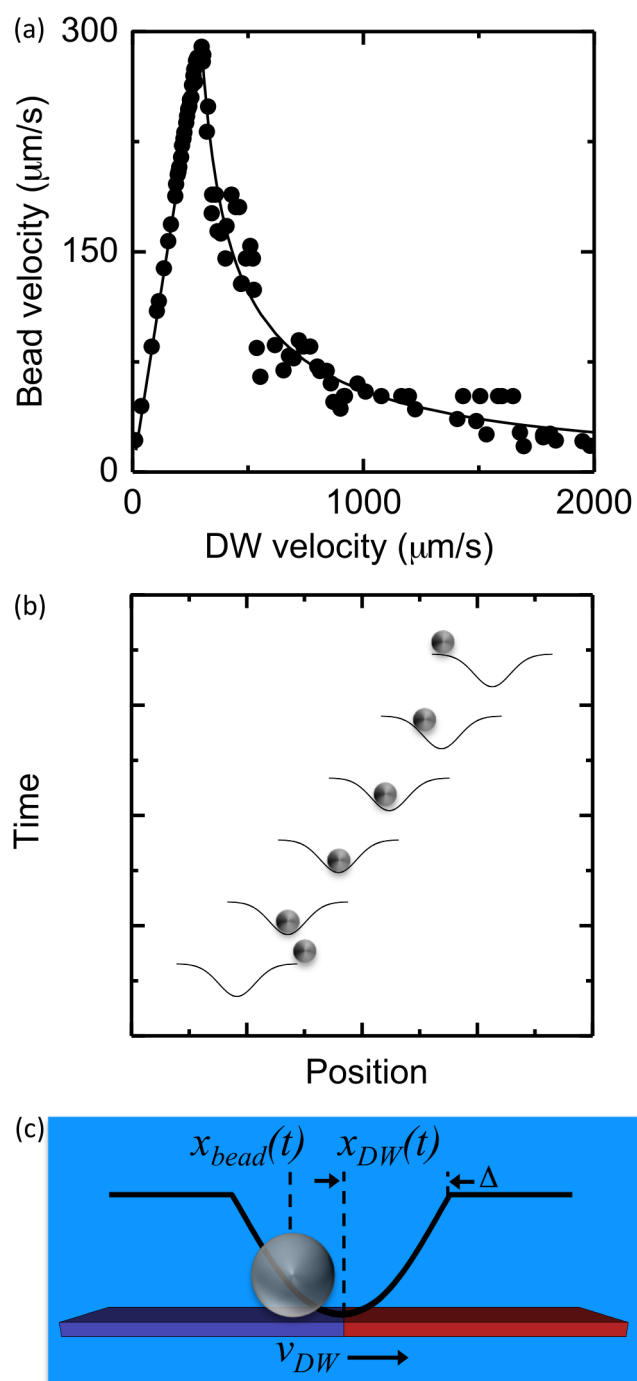


Figure 6

BB11981

30APR2013

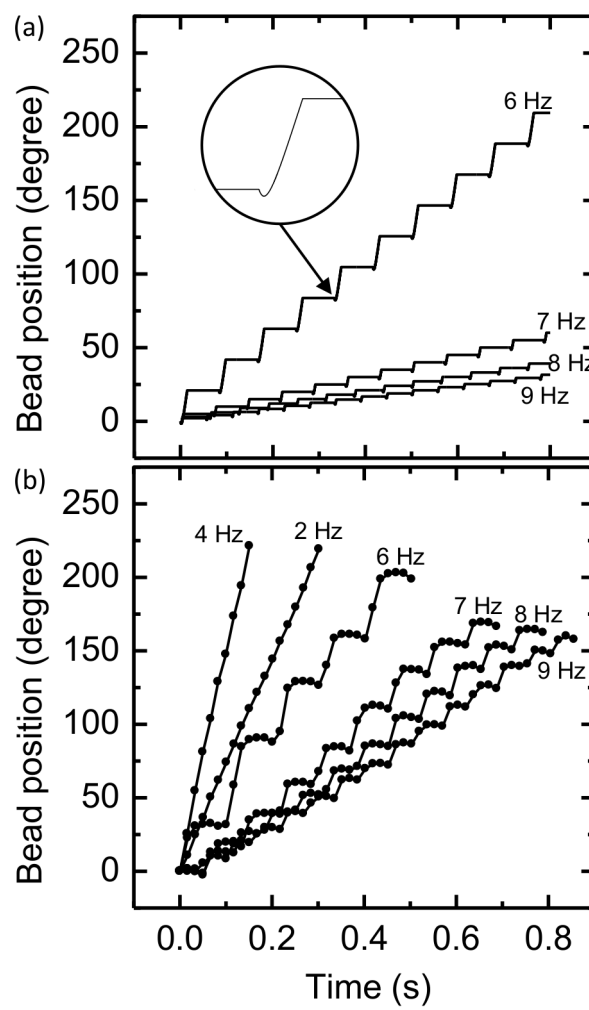


Figure 7

BB11981

30APR2013

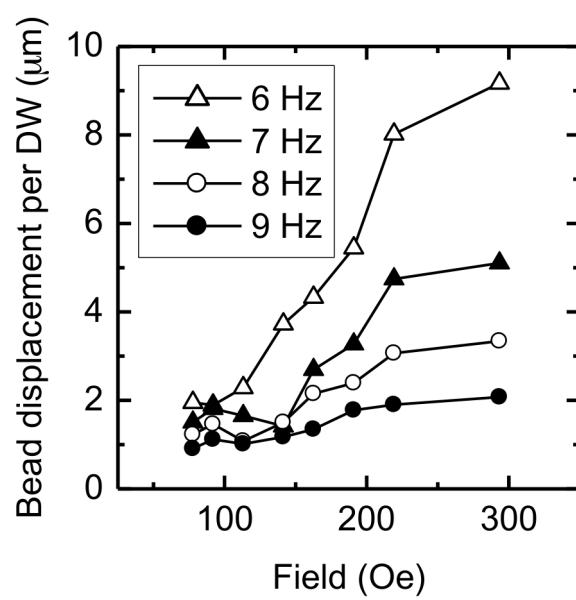


Figure 8

BB11981

30APR2013